Rafiee Fanood, Mohammad M. and Janssen, Maurice M. H. and Powis, Ivan (2016) Wavelength dependent photoelectron circular dichroism of limonene studied by femtosecond multiphoton laser ionization and electron-ion coincidence imaging. Journal of Chemical Physics, 145 (124320). 124320/1-124320/12. ISSN 1089-7690

Wavelength dependent photoelectron circular dichroism of limonene studied by femtosecond multiphoton laser ionization and electron-ion coincidence imaging

Mohammad M. Rafiee Fanood,[1,2] Maurice M.H. Janssen,[1,3] and Ivan Powis [4,*]

[1] LaserLaB Amsterdam, VU University Amsterdam, De Boelelaan 1081, 1081 HV Amsterdam, The Netherlands.

[2] Current address: Department of Imaging Physics, Delft University of Technology, Lorentzweg 1, 2628 CJ Delft, The Netherlands

[3] Current address: MassSpecpecD BV, Drienerbeeklaan 35,7522NA Enschede, The Netherlands

[4] School of Chemistry, University of Nottingham, Nottingham NG7 2RD, UK

*Corresponding Author:
Tel: +44 115 9513467
E-mail: ivan.powis@nottingham.ac.uk

Abstract

Enantiomers of the monoterpene limonene have been investigated by (2+1) resonance enhanced multiphoton ionization and photoelectron circular dichroism employing tuneable, circularly polarized femtosecond laser pulses. Electron imaging detection provides 3D momentum measurement while electron-ion coincidence detection can be used to mass-tag individual electrons. Additional filtering, by accepting only parent ion tagged electrons, can be then used to provide discrimination against higher energy dissociative ionization mechanisms where more than three photons are absorbed to better delineate the two photon resonant, one photon ionization pathway. The promotion of different vibrational levels and, tentatively, different electronic ion core configurations in the intermediate Rydberg states can be achieved with different laser excitation wavelengths (420 nm, 412 nm, and 392 nm), in turn producing different state distributions in the resulting cations. Strong chiral asymmetries in the lab frame photoelectron angular distributions are quantified, and a comparison made with a single photon (synchrotron radiation) measurement at an equivalent photon energy.

1. Introduction

Photoelectron circular dichroism (PECD) is a powerful and relatively novel technique to study the structural and electronic characteristics of chiral molecules.[1-3] Initially developed using synchrotron radiation[4-6], more recently the PECD technique has expanded its reach significantly by utilizing table-top ultrafast laser-based radiation.[7-13] It has been shown in the various chiral molecules studied by PECD that a pronounced forward-backward asymmetry in the photoelectron angular distribution can be observed, typically ranging from 1–40% of the total photoionization yield. This PECD asymmetry is two to three orders of magnitude larger than the typical asymmetry observed in (vibrational/electronic) circular dichroism. Furthermore, it was shown that the combination of PECD with correlated mass detection is able to provide direct enantiomer selectivity and quantitative data on the enantiomeric excess of chiral molecules in multi-component mixtures. [14] In two recent studies using both synchrotron-based single photon ionization and laser-based multiphoton ionization, it was shown that the quality of PECD measurements and the measurement of enantiomeric excess (e.e.) data has reached the 1% accuracy level.[15,16]

So far, little has been reported regarding the effect of laser wavelength on the measured PECD asymmetry in multiphoton excitation. Lehmann *et al.* [8] reported multi photon- (MP-) PECD data for laser excitation at 400 and 380 nm in camphor. The experimental MP-PECD data were interpreted as resulting from single photon ionization after two-photon resonant electronic excitation to 3s and 3p Rydberg states of camphor. Theoretical calculations and interpretation were presented that model the photoelectron angular distribution as a single photon ionization from a two-photon excited intermediate state with a non-isotropic distribution of molecular axes. For the camphor molecule qualitative agreement was observed between the experimental results and these theoretical calculations.

Here we report an extensive study on wavelength dependent MP-PECD results using laser-based multiphoton excitation and electron-ion coincidence imaging of the chiral molecule limonene. Limonene is possibly the most important member of the monoterpenes, being found, with varying

enantiomer ratios, in extracts and emissions from a great range of plant species — most notably of course in citrus fruits. There is evidence that changing enantiomer ratios emitted from coniferous forests may be indicative of plant stress conditions [17] and subsequent interactions in the biosphere (insects, animals) are known to be enantiospecific. Enantioselective detection of limonene clearly then has a role to play in understanding complex processes in our biosphere. [18] Limonene has also been detected in the marine environment[19] and it is ubiquitous in the modern urban environment, its enantiomers serving as odorants in many domestic products (including perfumes, cosmetic and cleaning agents, foodstuffs), an ecologically approved industrial degreasing fluid, and as a feedstock for various chemical manufacturing.

A first communication on PECD of limonene was reported recently for multiphoton excitation at 420 nm.[10] At this wavelength, ionization takes place via a vibrationally excited Rydberg state and PECD asymmetry of about 4.5 % was reported. In this publication, we present an extended study of multiphoton PECD of limonene at nominal wavelengths of 420, 412 and 392 nm. This paper is structured as follows. In Section 2 we briefly describe the experimental method and setup. In Section 3 we present and discuss the extensive experimental results obtained with the electron-ion coincidence imaging spectrometer reporting Time-of-Flight (ToF) mass spectra, photoelectron spectra (PES) of mass-selected ions, and PECD asymmetry at the various excitation wavelengths. In Section 4 we present our interpretation of the various multiphoton processes and also compare our laser-based multiphoton results with a recent synchrotron-based single photon PECD measurement of limonene. Finally we summarize our conclusions in Section 5.

2. Experimental

The electron-ion coincidence imaging spectrometer that was used in this work has been described in detail before[20,21] and we will only discuss the most relevant parts for the present study. A schematic of the set-up is shown in Fig. 1.

Liquid samples of limonene enantiomers were purchased from Sigma-Aldrich with a stated purity of 98% (S) and 99% (R). Enantiomeric excess (e.e.) of the R-(+) sample was stated to be >0.98 (hence effectively enantiopure) but no e.e. was specified or stated for the S-(-) sample. However, from the measured optical rotation of the two we estimate a probable S- enantiomer composition of only 85% — 90% (e.e. 0.7 — 0.8). The samples were held in an external stainless steel bubbler maintained at room temperature. A stream of pure Ne gas sweeps the sample vapor through a stainless steel transfer line to a 150 µm diameter nozzle in the source chamber. The Ne backing pressure was 0.2 bar for measurements at 420 nm and 412 nm and 0.6 bar for the measurement at 392 nm. The expanding gas mixture generates a continuous molecular beam in the source chamber. The molecular beam is doubly skimmed downstream from the nozzle as it passes through the buffer chamber into the imaging chamber. In the imaging chamber, the molecular beam interacts with laser light propagating perpendicularly. After ionization of the molecule, electrons are extracted by velocity map imaging (VMI) optics[22] toward a time-and position sensitive delay line detector. The full three dimensional momentum of each electron is directly obtained from its position and time of arrival. Ions are extracted downward toward the opposing delay line detector where only the time of arrival is recorded. Home-built high-voltage switches are used to change the magnitude and polarity of the high voltages on the ion lenses. The switches are operated at the repetition rate of the laser system (3 kHz). Both electron and ion time-of-flight (TOF) tubes are shielded by a 1mm thick µ-metal tube. The typical voltages on the charged particle lenses (repeller (R), extractor (E) and extra lens (L))

used for detecting electrons and ions are, respectively, R_e = -520 V, E_e = -385 V, L_e = -275 V and R_i = 2000 V, E_i = 1460 V, L_i = 0 V.

The commercial femtosecond laser system (Spectra Physics) consists of a Titanium:Sapphire oscillator (Mai-Tai) that seeds the chirped regenerative amplifier (Spitfire-Ace). The fundamental output of the laser was frequency doubled in a BBO crystal and this second harmonic pulse was used for multiphoton ionization of the limonene samples. In this work, three different laser wavelengths were used (420 nm, 412 nm, and 392 nm) with pulse characteristics that are summarised in Table 1. The laser beam was loosely focused into the molecular beam sample by a lens with *f*=30 cm to a spot size of approximately 100 µm × 150 µm. The corresponding intensity in the ionization volume is estimated to be 10^{11} – 10^{12} Wcm^{-2}. An achromatic quarter wave plate (B-Halle) was used to generate circularly polarized light. The polarization of the light was characterized in terms of the Stokes vector by the rotating quarter-wave plate method as described before.[8] The Stokes parameter describing circular polarization was determined to be $|S_3| > 0.98$ for all circular polarization states used in this study. With this excellent degree of polarization we judged it unnecessary to apply corrections for ellipticity to our results.

During the measurement, circular polarization (LCP/RCP) was switched every 500 s (1.5 million laser shots, MLS) in order to reduce potential effects of drift in laser intensity, signal stability and beam pointing. The measurement on each enantiomer was performed during 36 MLS at 420 nm, 45 MLS at 412 nm and 63 (58.5) MLS for R-(S-)limonene at 392 nm. All measurements were made recording data in electron-ion coincidence mode, and to minimise false coincidences laser and focussing conditions were chosen to restrict typical electron event count rates to < 0.08 per laser shot. After careful checks that the centre of the alternated electron images were the same, all files with the same polarization were combined together post measurement for data analysis. It should be noted that this does not then require 2D image inversion since with precise electron flight times being recorded the full 3D momentum distribution is directly available.

For comparison we also include here a measurement made, as part of a wider VUV investigation,[23] on the DESIRS[24] beamline at the French synchrotron facility SOLEIL, using the DELICIOUS III electron-ion double imaging spectrometer.[25] This also uses a double skimmed supersonic beam formed by seeding room temperature vapour of limonene in 0.5 bar He prior to expansion through a 70 µm nozzle. The PES and PECD were recorded for a photon energy of 9.5 eV following a procedure as previously described.[26]

3. Results

The current experiments develop on a preliminary report[10] of the 420 nm multiphoton PECD of limonene, now using a different configuration spectrometer that provides better ion mass resolution, and utilising additional photon energies with laser excitation at 420 nm, 412 nm and 392 nm. Fig. 2 shows the ion time-of-flight (TOF) mass spectra recorded under these conditions at the three wavelengths. For a given wavelength the TOF spectra were independent of enantiomer and the circular polarisation used for the measurement.

The dominant peak in all cases is clearly the limonene parent (136 amu), and when expanded the mass resolution reveals ^{13}C isotopomers (137, 138 amu) present at natural abundance. From the integrated peak areas we can quantify the parent ion abundance in the 392 nm spectrum as 35%,

falling to ~28% at 412 nm and 420 nm. Limonene has an ionization potential of 8.52 eV[27] and so energetically a minimum of three photons are required to ionize the sample at each wavelength considered (see Table 1). Figure 2 then also includes a single photon ion TOF spectrum recorded with synchrotron VUV radiation at the 392 nm three-photon equivalent energy of 9.5 eV. [23] In direct comparison with the 392 nm multiphoton spectrum (and also the 412 and 420 nm spectra), the single photon spectrum shows negligible fragmentation. This contrasts with an earlier synchrotron study[28] where limonene was observed to be 25% fragmented at 9.5 eV. However, due to differences in the molecular beam source in that earlier study (sample reservoir was elevated to 110° C, sample seeded in an Ar beam, and singly skimmed) internal cooling of the limonene was likely less efficient and complete, so that this was probably thermally induced fragmentation, a view supported by the observed tailing in the breakdown diagrams.[28] The cooling achieved in the multiphoton experiments reported here is likely to be comparable to that of the current synchrotron experiment, due to not now heating the sample reservoir and similar doubly skimmed beam source designs. In any event, the more extensive fragmentation seen with laser ionization is an indication that more than three photons may be being absorbed to provide sufficient energy.

Fig. 3 presents a recent[29] full valence region photoelectron spectrum (PES) of limonene recorded at modest resolution. Also marked are calculated ionization energies corresponding to production of various cation states. It can be seen that there is a high density of cation states sitting 3—4 eV above the lowest ion states at 8.5 — 9.5 eV. Consequently, it is feasible that in laser multiphoton ionization the uptake of further photons, leading to increased fragmentation, could occur in the manifold of singly excited ionic states, *after* an initial 3-photon ionization process. Such a cation photodissociation mechanism would not affect the recorded photoelectron spectra or angular distributions which precede it.

Fig. 4 displays the electron energy spectra of limonene derived from the full 3D electron momentum distribution recorded at each laser wavelength. For a given wavelength the electron distribution is essentially identical for either enantiomer, and for each circular polarization of the laser light. The dominant peaks occur at relatively low kinetic energies, although we defer detailed discussion of the structure. However, the spectra in the top row of the figure, that include all electrons without using coincidence ion mass filtering, show evidence of a tail to high energy that does not return to a zero baseline toward the right edge of the plot. These right side kinetic energies, however, exceed the available excess of the respective three photon energies (Table 1) over the expected 8.52 eV ionization energy of limonene.[27] The coincident ion mass-tagging provides more insight. The middle row spectra of Fig. 4, which are coincident with parent ion do not have this tail, and *do* return to a zero baseline, consistent with a three photon ionization mechanism. The high energy tailing, as judged from the bottom row of fragment ion-tagged spectra in Fig 4, evidently accompanies *some* production of fragment ions. Hence, while fragmentation of the parent ion may be enhanced by post-ionization absorption of photons, as discussed above, the evidence of fast electrons suggests that some proportion of the fragment ion yield alternatively results from a four (or more) photon ionization mechanism.

Coincidence detection of electrons can usefully be employed to discriminate against the yield from all higher energy ion fragmentation channels. While post-ionization uptake of excess photons should not adversely impact the study of ionization dynamics, and PECD in particular, we infer that coincidence detection of parent ion mass-tagged electrons provides a valuable means to guard

against potential higher photon order, above threshold ionization mechanisms and so permits better characterisation of the process being studied.

The PECD angular asymmetry for a given enantiomer and circular polarization is conveniently expressed [2,8,11] as

$$G = 4\left(\frac{F-B}{F+B}\right), \qquad \text{Eq. 1}$$

where *F* and *B* are, respectively, the number of electrons emitted into the forward and backward hemispheres (relative to the laser beam direction). By recording equal total counts for both polarizations the LCP and RCP data may be combined as a dichroism in such a way that any residual forward-backward instrumental asymmetry (which is independent of polarization) cancels out.[2,8,9] Hence, in Eq. 1 $F = N_{\mathrm{LCP,f}} + N_{\mathrm{RCP,b}}$ and $B = N_{\mathrm{LCP,b}} + N_{\mathrm{RCP,f}}$ where $N_{p,d}$ are the number of counts for polarization helicity *p* in direction *d*. The error in *G* is estimated by standard error propagation assuming Poisson statistics.

Fig. 5 provides a visual overview of the electron energy resolved PECD asymmetry results at each photon wavelength. For each data point counts in the range ±0.1 eV about the data point were included in evaluating the PECD using Eq. 1. The statistical errors shown are greater for the coincidence data (middle and bottom rows) due to the reduced number of coincident counts. In particular we note that the 420 nm data (left column) are in close agreement with our earlier data obtained at the same nominal laser wavelength.[10]

The normalised photoelectron angular distribution (PAD), $I_p(\theta)$, expected from an *n*-photon ionization of a chiral molecule with circular polarized light is given by [8]

$$I_p(\theta) = 1 + \sum_{i=1}^{2n} b_i^{\{p\}} P_i(\cos\theta), \qquad \text{Eq.2}$$

where *p* is the polarization of the light, and *p*=+1 and *p*=-1 correspond to left circular polarized (LCP) and right circular polarized (RCP), respectively. $P_i(\cos\theta)$ are Legendre polynomials, $b_i^{\{p\}}$ are the corresponding expansion coefficients, and θ is the angle between the electron momentum and the propagation direction of the laser beam. Switching the helicity of the circularly polarized light (or exchanging enantiomers) can be expected to generate a sign change of the odd Legendre coefficients while leaving the even Legendre coefficients unaltered. Thus the odd Legendre terms containing the chiral information can be isolated and extracted by examining the difference between two polarizations (LCP and RCP) for a single enantiomer: [8]

$$I_{lcp}(\theta) - I_{rcp}(\theta) = \sum_{i=1}^{n} 2b_{2i-1}^{\{+1\}} P_{2i-1}(\cos\theta) \quad , \qquad \text{Eq. 3a}$$

while even coefficients can be obtained from fitting the sum of the two data sets:

$$I_{lcp}(\theta) + I_{rcp}(\theta) = 2 + \sum_{i=1}^{n} 2b_{2i}^{\{+1\}} P_{2i}(\cos\theta) \qquad \text{Eq. 3b}$$

It also follows by taking Eq. 2 and integrating over the forward and back hemispheres to obtain expressions for the total count in either, that the asymmetry, *G* , appearing in Eq. 1 can be expressed in terms of the odd coefficients:[2,8]

$$G = 2b_1^{\{+1\}} - \tfrac{1}{2} b_3^{\{+1\}} + \tfrac{1}{4} b_5^{\{+1\}} - \ \ldots \qquad \text{Eq. 4}$$

The inclusion here of terms up to the 5th order coefficient is appropriate for an anticipated 3 photon process.

In Table 2 we summarise the results of fitting for the $b_i^{\{+1\}}$ coefficients using Eq. 3 and provide values for the asymmetries, *G*, calculated using alternatively a direct F/B count (Eq. 1) or the odd Legendre polynomial coefficients (Eq. 4). These coefficients and asymmetries are formed using the indicated ranges of electron kinetic energy, chosen as discussed below. Because of the uncertain S-enantiomer e.e., we only provide the R-enantiomer data in this quantitative analysis.

4. Discussion

The two outermost valence orbitals of limonene (Fig. 6) are C=C π orbitals, with the 2π (HOMO) and 1π (SHOMO) located in, respectively, the cyclohexene ring and isopropenyl tail of the molecule.[27] The conformational landscapes have been explored by a number of authors,[27,30,31] the more stable structures having the isopropenyl tail in an equatorial position. This leaves three possible dihedral angles for the tail group to adopt, structures which are conveniently labelled Eq-1, Eq-2, and Eq-3 in decreasing order of stability.[30] We will henceforth adopt shortened notation, such as …$1\pi^2 2\pi^2$, when describing the electronic configuration of limonene states.

4.1 Rydberg intermediate states

In Fig. 7 we show the gas phase VUV absorption[27,32] and circular dichroism[32] (CD) spectra of limonene. The absorption starts around 225 nm (below 5.6 eV) with a low pedestal region, which nevertheless shows some vibrational structure (more prominent in the CD spectrum). Brint et al.[32] assigned the first feature, at 218 nm (5.69 eV), to excitation from the 2π HOMO and identified the upper level as the 3*s* Rydberg state, based upon the observed 22915 cm^{-1} term value of this excitation. The further weak structures at 210 nm (5.90 eV) and 204.9 nm (6.051 eV) were assigned to the same electronic transition with one or two quanta of vibrational excitation, probably in the ring C=C stretching mode. This vibrational assignment is very plausible given the localisation of the excited 2π electron, the estimated frequency of ~1700 cm^{-1} for this mode in the neutral,[31] and the slightly reduced vibrational frequency of ~1500 cm^{-1} observed in the Rydberg spectrum.[32]

The limonene Rydberg state energies have been examined employing either EOM-CCSD quantum molecular calculations[27] or, alternatively, time dependent density functional methods with range corrected functionals,[10] in both cases using augmented cc-pVDZ basis functions. Both series of calculations show some systematic over-estimation of the Rydberg excitation energies. We have discussed this more fully in previous work[10] but concluded that the empirically based assignment of the first $2\pi \rightarrow 3s$ excitation offered by Brint et al.[32] was correct. In Fig. 7 we show, for each conformer Eq-1 — Eq-3, our preferred adjusted[10] CAM-B3LYP/dAug-cc-pVDZ transition energies and oscillator strengths.

Also marked in Fig. 7 are the two-photon-equivalent energies and estimated two-photon excitation bandwidths for the three laser wavelengths reported in the current work. Since these all fall in the

broad absorption continuum around 200 nm it is plausible that our measurements can be resonantly enhanced at the two-photon level. More particularly, the nominal 420 nm excitations (very slightly to the red of our preliminary limonene MP-PECD study[10]) correspond to the transition $2\pi(v=0) \rightarrow 3s$ (v = 1), while at 412 nm the two-photon excitation can be assigned as $2\pi(v=0) \rightarrow 3s$ (v = 2); the 392 nm excitation lies above the threshold for both $2\pi \rightarrow 3p(v^*)$ and $1\pi \rightarrow 3s(v^*)$ transitions.

4.2 Cation states

The first band of the photoelectron spectrum of limonene is shown in detail in Fig. 8, where we compare a high resolution He I PES[27] with the VUV ($h\nu$ = 9.5 eV) electron spectrum recorded by velocity map imaging (VMI-PES) at the Soleil synchrotron.[23] As can be seen from the calculated vertical ionization energies marked on the overview spectrum (Fig. 3), the observed band is expected to encompass both the $2\pi^{-1}$ and $1\pi^{-1}$ ionizations, although due to the overlapping neither the vertical, nor of course the adiabatic, ionization energies of the latter SHOMO ionization can be readily identified. The broad similarities of the He I and VMI PES are clear, but it may be noticed that the minor peaks that appear between the major "progression" in the He I PES are absent in the VMI PES. This apparent loss may be partially explained by a smearing out of detail attributable to the lower resolution achieved in the VMI technique. However, one other significant experimental difference is temperature; the He I spectrum is a room temperature measurement, while the VMI PES is recorded with a jet-cooled sample. Differences may thus potentially be ascribed to collapse of the anticipated conformer population in the VMI molecular beam experiment.

Fig. 8 includes a Franck-Condon simulation for the $2\pi^{-1}$ ionization of the single Eq-1 ground state conformer of limonene. Vibrational parameters for the neutral and cation of the ground state Eq-1 conformer were obtained from an MP2/cc-pVDZ calculation using the program Gaussian 09,[33] and the harmonic frequencies were scaled by a factor 0.93. Franck-Condon factors were obtained using the FC-Lab II software package.[34] This simulation provides a clear understanding for the first three prominent peaks occurring in the low energy region of the PES band, below ~9eV. Although each is an unresolved superposition of several individual vibrational transitions, these basically comprise progressions in the ring C=C stretch mode (scaled ω_e^+ = 1479 cm^{-1}) in combination with other low frequency modes, notably 0—2 quanta of the M1 methyl's torsional motion (scaled ω_e^+ =111 cm^{-1}). We note that Smialek et al.[27] report vanishingly small Franck-Condon factors for ionization of this Eq-1 conformer as a consequence of the very large change in dihedral angle of the M2 methyl group (relative to the ring plane) in their calculated cation geometry (-108° → -89°). We have unsuccessfully attempted to replicate this finding using various DFT, MP2, and CASSCF calculations, but the predicted change in dihedral angle was never more than a few degrees.

Above ~9 eV a clear discrepancy between vibrational simulation for the HOMO $2\pi^{-1}$ channel and the experiment emerges, coinciding with the expected onset of the $1\pi^{-1}$ ionization channel. Calculated vertical ionization energies for this SHOMO ionization are around 8.9 eV,[27] although the next prominent maximum in the experimental spectra (from which a vertical IP could be inferred) is higher, at 9.1 eV. A full understanding of the observed profile on the high energy side of the combined PES band requires a more complex analysis, including assessment of possible vibronic interaction between this close-lying pair of electronic states; nevertheless it seems a reasonable supposition that the peak at ~9.1 eV can be largely associated to the second, $1\pi^{-1}$, ionization channel.

4.3 Ionization pathways

We are now able to consider the overall ionization schemes at each studied wavelength, which we do by following and extending the arguments previously developed in our preliminary 420 nm investigation of limonene.[10]

4.3.1 420 nm

The preceding analysis of VUV and photoelectron spectra indicates that at 420 nm there is a 2-photon resonant enhancement by excitation via the $1\pi^2 2\pi^1 3s^1$ Rydberg state having one quantum of the ring C=C stretching mode vibration. Given the similar frequencies inferred for this mode in the Rydberg intermediate (1500 cm^{-1})[32] and the 1479 cm^{-1} deduced for the ground electronic state in our Franck-Condon simulation above, invoking a Δv=0 propensity rule for the Rydberg ionization seems well justified, so that the resulting cation is likely in the $X\ 1\pi^2 2\pi^1$ ($v^+_{C=C}$=1) state. Considering the three-photon equivalent energy and bandwidth (Table 1) and the 8.521 eV adiabatic ionization energy[27] then suggests an electron kinetic energy of 0.15±0.02 eV . This calculation can be seen schematically in Fig. 8 by reading off the position of the nominally $v^+_{C=C}$=1 VMI-PES peak against the 420 nm equivalent electron energy scale marked along the top, while Fig. 9 offers a more conventional schematic energy level view of this discussion.

The 420 nm PES (Fig. 4) peaks at ~0.1 eV, broadly in line with the calculation for the $v^+_{C=C}$=1 level, and so corroborating this prediction of the dominant assignment for the 420 nm ionization mechanism.

4.3.2 412 nm

The principal peak in the 412 nm PES (Fig. 4) now sits at ~0.15 eV. This upward shift corresponds closely to the increase in just the single photon energy when moving from 420 nm to 412 nm, rather than the net three-photon equivalent energy increase. From this we can infer that any extra energy pumped into the two photon resonant neutral intermediate remains embedded in the cation, according with the Δv=0 propensity rule for Rydberg ionization. Having identified the most likely intermediate as the $1\pi^2 2\pi^1 3s^1$ ($v_{C=C}$=2) state from the discussion of the VUV spectra (Section 4.1), we can conclude the cation produced to be dominantly in the $X\ 1\pi^2 2\pi^1$ ($v^+_{C=C}$=2) state, and again this could also be inferred from the alignment of the nominal $v^+_{C=C}$=2 VMI-PES peak with 0.15 eV on the 412 nm equivalent electron energy scale in Fig. 8.

There is, however a second small feature at ~0.45 eV in the 412 nm PES (Fig. 4), best seen in the parent ion coincident data which, as argued in Section3, gives the cleanest view of the three-photon ionization mechanism. Energetically this corresponds to the expected electron energy (0.5±0.02 eV) at the adiabatic ionization limit (v^+=0); once again this can also be read off on the 412 nm energy scale as the position of the first in the VMI-PES (Fig. 8) and represents a weakening of the Δv=0 propensity rule.

The principal PES peak at 412 nm also appears a little wider than that at 420 nm. While there is no clear additional structure visible in Fig. 4, we cannot then preclude the possibility of an unresolved contribution from ionization to vibrational levels sitting between the just discussed v^+=0 and $v^+_{C=C}$=2 states, and so can speculate that $v^+_{C=C}$=1 may also be formed. Fig.9 includes a schematic view to summarise this discussion.

On purely energetic grounds the excited A state cation (IP ≈ 8.9 eV) would be accessible (3×412 nm ≅ 9.02 eV), also then providing ~0.1 eV excess energy for the photoelectron. But the two photon equivalent energy at 412 nm is insufficient for the intermediate $1\pi \rightarrow 3s$ Rydberg excitation. Consequently, it seems reasonable to discount resonant ionization to the excited A state at this wavelength as it would require a two electron excitation from the neutral Rydberg, $1\pi^2 2\pi^1 3s^1 \rightarrow 1\pi^1 2\pi^2 + e^-$.

4.3.3 392 nm

The principal peak in the 392 nm PES (Fig. 4) now sits at 0.4 eV, so a shift of 0.25 eV relative to the 412 nm data, or 0.3 eV relative to the 420 nm PES. These shifts no longer match the increase in single photon energy as the wavelength is changed, which may indicate a different ionization pathway applies. The intermediate state assignment cannot be inferred from the VUV spectra (Fig. 7), which have no distinct structure in this region, but the two photon excitation energy now sits above the expected adiabatic thresholds for $1\pi^2 2\pi^1 3s^1$, $1\pi^2 2\pi^1 3p^1$, and $1\pi^1 2\pi^2 3s^1$ Rydberg states. While all could therefore serve as vibrationally excited intermediates for the ionization, the latter is particularly interesting because of the different configuration of the Rydberg core. It can be expected to ionize to the first electronically excited *A* $1\pi^1 2\pi^2$ cation state. The adiabatic ionization energy of this $1\pi^{-1}$ state is not precisely known, as previously mentioned (Section 4.2), but with a likely vertical IP of ~8.9 eV it is comfortably accessible, energetically, in a three photon ionization.

A comparison between the 392 nm PES and the VUV PES is then revealing, as the peak energy, 0.4 eV, in the former clearly correlates with the fourth peak in the VUV spectrum (Fig. 8) and this, we have noted, is not a member of the progression in the ring C=C stretching mode of the X state but has a much more complex structure involving a major contribution from the *A* state $1\pi^{-1}$ ionization channel. We thus infer that at 392 nm the 0.4 eV PES peak results from production of the electronically excited cation. Taking a tentative estimate[10] of 6.12 eV for the transition to the Rydberg $1\pi^1 2\pi^2 3s^1$ state, and the two-photon equivalent energy at 392 nm (Table 1) suggests a vibrational excitation of 0.2 eV in the $1\pi^{-1}$ Rydberg core that is produced. This excitation is approximately equivalent to one quantum of a C=C stretching mode which here it seems would most plausibly be expected to be that of the isopropenyl tail, with a similar deduction following for the $1\pi^{-1}$ cation that ultimately results. However, just as in the VUV study, we cannot entirely rule out some minor contribution from the electronic ground state $2\pi^{-1}$ ionization with ill-determined excitation of vibrational modes in the Rydberg and cation states.

The second feature in the 392 nm PES, seen most clearly in the parent ion coincident data (Fig 4) is a distinct peak at 1 eV. This is readily attributed to ionization at the first adiabatic ionization threshold (8.52 eV) by energetic arguments and hence corresponds to production of vibrationless *X* $2\pi^{-1}$ cation. Filling in of the spectrum between the 0.4 eV and 1.0 eV peaks suggests that there may again be unresolved some minor contributions from the production of excited vibrational states of the *X* $2\pi^{-1}$ cation.

4.4 Photoelectron Circular Dichroism

It is now possible to examine trends in the recorded PECD data, guided by the possible assignments of regions of the electron energy spectrum to the ionizing Rydberg state and final cation state. For convenience we will use a single quantum number, v^+ , to designate the ion vibrational state

assignment, predominantly to C=C stretching modes, while recognising that this simplifies a likely much more complex vibrational structure involving various other modes. Focussing for the moment on the top row of non-coincident PECD data in Fig. 5, where the statistics are better, one sees at all wavelengths commensurate PECD asymmetries, *G*, of magnitude in the range 0—5%. At a given wavelength there is a slow shift in the R-enantiomer asymmetry from negative towards more positive values (opposite for the S-enantiomer as anticipated due to the chiral mirroring) as the assigned vibrational levels decrease and/or the electron energy correspondingly increases. At 412 nm as the assigned v^+ varies $2 \rightarrow 0$ the PECD magnitude falls effectively to zero, or perhaps even displays a slight reversal. In comparison the $v^+=0$ peak observed at much higher kinetic energy (in the 392 nm data) now displays a clear reversal of the PECD asymmetry, in itself a rather dramatic overall change, although possibly just a continuation of the trend already noted. On the other hand the peaks assigned as $2\pi^{-1}$ $v^+=1$ (420 nm) and $2\pi^{-1}$ $v^+=2$ (412 nm) display comparable PECD asymmetry at essentially similar electron kinetic energy (≈0.1 eV), which does not immediately suggest a pronounced vibration level-dependent PECD effect. In summary the vibrational dependence of the PECD is probably weak, but such effects cannot as yet be disentangled from simpler electron kinetic energy dependent variations that can be expected.[3]

In Fig. 10 we present the PES and PECD recorded with a single 9.5 eV VUV photon at the SOLEIL synchrotron.[23] The assignment of the PES has already been discussed (see Fig. 8 and Section 4.2) and adopting a shorthand notation the peaks are labelled as $v^+=0$, 1, 2 of the ground electronic state; the fourth peak (ionization energy 9.1 eV) does not continue this progression and, we deduce, includes significant contribution from ionization to the vibrationally excited *A* $1\pi^{-1}$ cation. The VUV PECD (lower panel Fig. 10) is strongly modulated in a manner which correlates with the vibrational structure of the PES. The peak values of the PECD corresponding to $v^+=0$, 1, 2 are in the range 1—5%, and decrease with increasing vibrational level, just as has been noted above for the MP-PECD data. On the other hand, with single photon excitation the corresponding electron energy must, of course, strictly *decrease* with increasing v^+. This might hint at a vibrational dependence rather than electron kinetic energy variations being responsible for the diminishing PECD.

In the region of the fourth *A* $1\pi^{-1}$ PES peak the PECD asymmetry reverses to reach similar, but negative, values. We comment that it is not uncommon in VUV PECD studies to find ionization of adjacent orbitals happens to yield PECD of opposite signs.[26,35,36]

Fig. 10 is also used to facilitate a comparison of the 392 nm and VUV results. The three-photon equivalent energy (9.48 eV) is virtually identical to the single VUV photon energy (9.5 eV) so that these data can be presented on a common energy scale. First, from the superimposed presentation of the PES it is perhaps easier to see the effect of the parent ion coincidence tagging in cleaning-up the multiphoton spectra and attenuating the high energy $n_{photon}>3$ induced tail. Secondly, despite the worsened statistics of the coincidence data the MP-PECD absolute magnitude (middle panel Fig. 10) appears to be attenuated if $n_{photon}>3$ contribution is *not* filtered out. Thirdly, there is a striking match between the first and fourth peaks ($2\pi^{-1}$ ($v^+=0$) and $1\pi^{-1}(v^+ \geq 1)$) in the VUV PES and the principal structure in the multiphoton PES, which suggests a common interpretation. This strong similarity applies equally to the PECD and MP-PECD data, albeit the energy resolution is poorer in the MP-PECD data. Specifically, one sees both data sets have ~5% asymmetry around the first $2\pi^{-1}$ ($v^+=0$) peak, dropping, then reversing to a similar absolute value in the vicinity of the highest energy peak. Since in the VUV we associate this latter structure principally with formation of the *A* $1\pi^{-1}(v^+ \geq 1)$

state cation these strong similarities could suggest the alternative interpretation of the 1 eV 392 nm peak, discussed above, is correct; namely ionization occurs via the Rydberg state with a $1\pi^1 2\pi^2$ core and leads to excited A state cation.

Is such comparison of PECD and MP-PECD results too facile? The ion cores of the two Rydberg states are the *X* $2\pi^{-1}$ and *A* $1\pi^{-1}$ cation states. In a sudden approximation for the ionization the emitted HOMO and SHOMO electrons (single photon case) and the Rydberg electrons (multiphoton case) will scatter off the same two ion core potentials. The importance of such final state scattering in PECD is well established,[6,37] it is after all how the photoelectron from a strongly localised, essentially achiral initial orbital senses the chirality of the molecule as it departs. On the other hand, the initial orbital enters into the dipole matrix elements and is not without influence. Pragmatically, the scattering of an electron from a localised C=C π orbital (as in the HOMO and SHOMO VUV ionizations) might well be expected to differ from that of one ejected from a diffuse Rydberg orbital; in which case the similarity seen between PECD and MP-PECD under otherwise comparable conditions is *a priori* surprising.

Another objection would be that the greater number of photons absorbed in the MP-PECD measurements can induce additional anisotropy. More insight is obtained by examining the harmonic composition of the PAD, and Table 2 provides a breakdown for the principal PES peaks using fitted Legendre polynomial coefficients, $b_i^{\{p\}}$ (Eq. 2). The PECD asymmetries, G, using the $b_i^{\{p\}}$ coefficients (Eq. 4) are also compared in the Table with those obtained across these same electron energy ranges from the simpler forward-backward scattering analysis (eq. 1) with excellent agreement being apparent. Excluding, for the moment, the data in the final column of Table 2, the PAD decompositions reveal that the greatest contribution to chiral asymmetry resides in the first $b_1^{\{p\}}$ coefficient for these MP-PECD measurements, as of course it also must for the single photon PECD. The higher *i* =3,5 coefficients are relatively small, and this is especially evident in the parent mass filtered data, which we have argued provides the cleaner view of the (2+1) REMPI ionization mechanism. Indeed, the higher order odd coefficients at 420 nm and 412 nm are seen in the mass-filtered case to be effectively zero (within the deduced error limits).

This contrasts with the situation encountered with an earlier (2+1) MP-PECD study of camphor where the absolute magnitude of b_3 was comparable to, or even exceeded, that of b_1 , and was semi-quantitatively predicted by a model considering one-photon ionization from an optically aligned intermediate. [8] Before inferring a non-aligned limonene intermediate from the lack of higher order chiral asymmetry it is salutary to examine the even coefficients where the *i* =2,4 values are clearly non-negligible. Non-zero coefficients for *i* >2 cannot arise in the one photon case, thus there is a clear signature of the multiphoton character in the even PAD terms, even while the odd (chiral) terms are more ambiguous.

Turning, finally, to examine the fast electron channel in the 392 nm data (last column Table 2) the b_3 coefficient does appear to take on a bigger magnitude relative to b_1 (as also, in the m/z 136 tagged 392 nm data, does b_5) but the limited statistical quality of the reduced size coincident data sets precludes a more extensive discussion at this point.

5. Conclusions

We have reported a (2+1) resonance enhanced multiphoton ionization and photoelectron circular dichroism study of jet-cooled limonene. Utilising electron-ion coincidence detection the photoelectron distributions can be filtered. Accepting only electrons that have been coincidence mass-tagged against undissociated parent ion provides additional discrimination against background contributions from higher energy ($n_{photon} > 3$) ionization pathways, better defining the ionization mechanism. Extending our first MP-PECD study made at two wavelengths (camphor[8]) three different laser wavelengths have been used here for limonene. This additional experimental variable was exploited to provide additional selectivity in vibrational state, and (tentatively) the electronic configuration of the Rydberg core, in the 2-photon excited resonant intermediate. One thus aims to obtain further insight into the role of the intermediate state in MP-PECD.

Perhaps the most obvious outcome is that, because of a Δv=0 propensity rule for Rydberg ionization, the final cation vibrational state can be controlled and selected. In VUV ionization it has been shown[38] that specific electron-nuclear coupling may dramatically modify the observed photoelectron asymmetry, and while nothing so extreme was noted here the potential exists for such effects to be observed either implicitly or explicitly. The use of narrower bandwidth, longer duration (ps) laser pulses would enhance vibrational resolution, and opens additional new possibilities, for example for selective conformer specific ionization through the resolved vibrational structure at the intermediate.[39]

Greater spectroscopic resolution would also enhance the possibilities for selecting the electronic configuration of the Rydberg state, and hence the cation state generated. The current understanding for limonene is limited by a lack of resolved structure in the available VUV Rydberg absorption spectrum[27,32], and correspondingly in the photoelectron spectrum, where the two outer electron bands overlap . The current MP-PECD results are, however, quite surprisingly analogous to the VUV single photon PECD in this region. The evidence as yet points to similar dichroism based only on considering the electronic state of the cation, regardless of whether the electron is ionized directly (VUV) or indirectly (REMPI) via initial promotion to a 3*s* Rydberg orbital. It is surprising because the valence π orbitals are highly localised, whereas a 3*s* Rydberg orbital is strongly delocalised, and this would be expected to provoke observable differences in the photoelectron scattering dynamics, and hence between PECD and MP-PECD at a given nett energy. In practice for limonene the $2\pi^{-1}$ and $1\pi^{-1}$ direct ionization channels probably occur in parallel above the $1\pi^{-1}$ ionization threshold, and the deeper issue of vibronic interaction between these states requires investigation. Similar caveats may be applied to the 392 nm REMPI process examined here.

Detailed analysis of the PADs, using the fitted Legendre polynomial coefficients, b_i , (Eq. 2) has shown that for all but the 392 nm 1 eV kinetic energy result the chiral b_3 and b_5 coefficients are effectively zero, to within close to the statistical uncertainty. This contrasts with studies of camphor, where the magnitude of b_3 is comparable to that of b_1[8,11] although it parallels observations on MP-PECD of methyl oxirane.[9] Intuitively, $b_3 \approx 0$ might appear to suggest no multiphoton character, or at least that the 2-photon intermediate was not aligned, so contributed no additional anisotropy. Yet this supposition is disproved by non-zero values obtained for the higher order even coefficients, b_4 and b_6. Evidently, having $n_{photons} > 1$ is a necessary, but not sufficient, condition for the observation of non-zero higher Legendre terms P_i where $i \geq 2$. Inferring ionization mechanisms from the

presence or absence of expected polynomials in the PAD needs then to be approached with caution. In detail the reasons for this are unclear, and further theoretical modelling is required to understand why this limitation is encountered for limonene, methyl oxirane,[9] and fenchone,[12] but not camphor.[8,11]

Acknowledgments

This research was financially supported by the council for Chemical Sciences of the Netherlands Organization for Scientific Research (NWO-CW VICI and CW-BAZIS) and the Marie Curie Initial Training Network ICONIC. IP further received funding from the EC Seventh Framework Programme – Access to Research Infrastructures – LASERLAB-EUROPE (proposal LLAMS-1957) and CALIPSO (Soleil beamtime proposal 20140139). Some computational resources were provided by the EPSRC UK National Service for Computational Chemistry Software (project CHEM559). Excellent technical support by R. Kortekaas in the construction of the Amsterdam imaging mass spectrometer and supporting experimental apparatus is gratefully acknowledged. We particularly thank Gustavo Garcia and Laurent Nahon for their assistance recording the VUV data, and J.-F. Gil for technical help, on the DESIRS beamline endstation at Synchrotron Soleil. We also thank the general SOLEIL staff for the smooth running of that facility. Finally we are grateful to Stefan Lehmann for fruitful discussions about the limonene MP-PECD data analysis.

References

[1] I. Powis, in *Advances in Chemical Physics*, edited by J. C. Light (Wiley, New York, 2008), Vol. 138, pp. 267.

[2] M. H. M. Janssen and I. Powis, Phys. Chem. Chem. Phys. **16**, 856 (2014).

[3] L. Nahon, G. A. Garcia, and I. Powis, J. Electron Spectrosc. Relat. Phenom. **204**, 322 (2015).

[4] N. Böwering, T. Lischke, B. Schmidtke, N. Müller, T. Khalil, and U. Heinzmann, Phys. Rev. Lett. **86**, 1187 (2001).

[5] G. A. Garcia, L. Nahon, M. Lebech, J. C. Houver, D. Dowek, and I. Powis, J. Chem. Phys. **119**, 8781 (2003).

[6] U. Hergenhahn, E. E. Rennie, O. Kugeler, S. Marburger, T. Lischke, I. Powis, and G. Garcia, J. Chem. Phys. **120**, 4553 (2004).

[7] C. Lux, M. Wollenhaupt, T. Bolze, Q. Q. Liang, J. Kohler, C. Sarpe, and T. Baumert, Angew. Chem.-Int. Edit. **51**, 5001 (2012).

[8] C. S. Lehmann, N. B. Ram, I. Powis, and M. H. M. Janssen, J. Chem. Phys. **139**, 234307 (2013).

[9] M. M. Rafiee Fanood, I. Powis, and M. H. M. Janssen, J. Phys. Chem. A **118**, 11541 (2014).

[10] M. M. Rafiee Fanood, M. H. M. Janssen, and I. Powis, Phys. Chem. Chem. Phys. **17**, 8614 (2015).

[11] C. Lux, M. Wollenhaupt, C. Sarpe, and T. Baumert, ChemPhysChem **16**, 115 (2015).

[12] C. Lux, A. Senftleben, C. Sarpe, M. Wollenhaupt, and T. Baumert, J. Phys. B **49**, LT201 (2016).

[13] A. Ferré, C. Handschin, M. Dumergue, F. Burgy, A. Comby, D. Descamps, B. Fabre, G. A. Garcia, R. Géneaux, L. Merceron, E. Mével, L. Nahon, S. Petit, B. Pons, D. Staedter, S. Weber, T. Ruchon, V. Blanchet, and Y. Mairesse, Nat. Photon. **9**, 93 (2015).

[14] M. M. Rafiee Fanood, N. B. Ram, C. S. Lehmann, I. Powis, and M. H. M. Janssen, Nat. Commun. **6**, 7511 (2015).

[15] L. Nahon, L. Nag, G. A. Garcia, I. Myrgorodska, U. Meierhenrich, S. Beaulieu, V. Wanie, V. Blanchet, R. Géneaux, and I. Powis, Phys. Chem. Chem. Phys. **18**, 12696 (2016).

[16] A. Kastner, C. Lux, T. Ring, S. Zullighoven, C. Sarpe, A. Senftleben, and T. Baumert, ChemPhysChem **17**, 1119 (2016).

[17] N. Yassaa and J. Williams, J. Chromatogr. A **1141**, 138 (2007).

[18] W. Song, M. Staudt, I. Bourgeois, and J. Williams, Biogeosciences **11**, 1435 (2014).

[19] N. Yassaa, I. Peeken, E. Zollner, K. Bluhm, S. Arnold, D. Spracklen, and J. Williams, Environ. Chem. **5**, 391 (2008).

[20] A. Vredenborg, C. S. Lehmann, D. Irimia, W. G. Roeterdink, and M. H. M. Janssen, ChemPhysChem **12**, 1459 (2011).

[21] A. Vredenborg, W. G. Roeterdink, and M. H. M. Janssen, Rev. Sci. Instrum. **79**, 063108 (2008).

[22] A. T. J. B. Eppink and D. H. Parker, Rev. Sci. Inst. **68**, 3477 (1997).

[23] M. M. Rafiee Fanood, PhD Thesis, VU University, Amsterdam (2015).

[24] L. Nahon, N. d. Oliveira, G. Garcia, J. F. Gil, B. Pilette, O. Marcouille, B. Lagarde, and F. Polack, J. Synchrotron Rad. **19**, 508 (2012).

[25] G. A. Garcia, B. K. C. de Miranda, M. Tia, S. Daly, and L. Nahon, Rev. Sci. Instrum. **84**, 053112 (2013).

[26] L. Nahon, G. A. Garcia, C. J. Harding, E. A. Mikajlo, and I. Powis, J. Chem. Phys. **125**, 114309 (2006).
[27] M. A. Smialek, M. J. Hubin-Franskin, J. Delwiche, D. Duflot, N. J. Mason, S. Vronning-Hoffmann, G. G. B. de Souza, A. M. F. Rodrigues, F. N. Rodrigues, and P. Limao-Vieira, Phys. Chem. Chem. Phys. **14**, 2056 (2012).
[28] G. A. Garcia, L. Nahon, and I. Powis, Int. J. Mass. Spec. **225**, 261 (2003).
[29] I Powis and S Turchini, to be published
[30] J. R. A. Moreno, T. R. Huet, and J. J. L. Gonzalez, Struct. Chem. **24**, 1163 (2013).
[31] F. Partal Urena, J. R. Aviles Moreno, and J. J. Lopez Gonzalez, Tet. Asym. **20**, 89 (2009).
[32] P. Brint, E. Meshulam, and A. Gedanken, Chem. Phys. Lett. **109**, 383 (1984).
[33] M. J. Frisch, G. W. Trucks, H. B. Schlegel, G. E. Scuseria, M. A. Robb, J. R. Cheeseman, G. Scalmani, V. Barone, B. Mennucci, G. A. Petersson, H. Nakatsuji, M. Caricato, X. Li, H. P. Hratchian, A. F. Izmaylov, J. Bloino, G. Zheng, J. L. Sonnenberg, M. Hada, M. Ehara, K. Toyota, R. Fukuda, J. Hasegawa, M. Ishida, T. Nakajima, Y. Honda, O. Kitao, H. Nakai, T. Vreven, J. J. A. Montgomery, J. E. Peralta, F. Ogliaro, M. Bearpark, J. J. Heyd, E. Brothers, K. N. Kudin, V. N. Staroverov, T. Keith, R. Kobayashi, J. Normand, K. Raghavachari, A. Rendell, J. C. Burant, S. S. Iyengar, J. Tomasi, M. Cossi, N. Rega, J. M. Millam, M. Klene, J. E. Knox, J. B. Cross, V. Bakken, C. Adamo, J. Jaramillo, R. Gomperts, R. E. Stratmann, O. Yazyev, A. J. Austin, R. Cammi, C. Pomelli, J. W. Ochterski, R. L. Martin, K. Morokuma, V. G. Zakrzewski, G. A. Voth, P. Salvador, J. J. Dannenberg, S. Dapprich, A. D. Daniels, O. Farkas, J. B. Foresman, J. V. Ortiz, J. Cioslowski, and D. J. Fox, Gaussian 09 Revision D.01 (Gaussian Inc., Wallingford, CT, 2013).
[34] I. Pugliesi and K. Muller-Dethlefs, J. Phys. Chem. A **110**, 4657 (2006).
[35] I. Powis, C. J. Harding, G. A. Garcia, and L. Nahon, ChemPhysChem **9**, 475 (2008).
[36] S. Daly, I. Powis, G. A. Garcia, H. Soldi-Lose, and L. Nahon, J. Chem. Phys. **134**, 064306 (2011).
[37] C. J. Harding, E. A. Mikajlo, I. Powis, S. Barth, S. Joshi, V. Ulrich, and U. Hergenhahn, J. Chem. Phys. **123**, 234310 (2005).
[38] G. A. Garcia, L. Nahon, S. Daly, and I. Powis, Nat. Commun. **4**, 2132 (2013).
[39] A. Hong, C. M. Choi, H. J. Eun, C. Jeong, J. Heo, and N. J. Kim, Angew. Chem.-Int. Edit. **53**, 7805 (2014).

Tables

Table 1 Laser parameters , together with *n*-photon equivalent energies

Laser λ	FWHM	Pulse[a]	limonene	1-photon		2-photon		3-photon	
		Energy	enantiomer	E	ΔE	E	ΔE	E	ΔE
nm	nm	μJ		eV	meV	eV	meV	eV	meV
420.34	2.47	16–20	R	2.950	17.3	5.899	24.5	8.849	30.0
420.33	2.51	15–16	S	2.950	17.6	5.899	24.9	8.849	30.5
412.54	2.47	20–23	R	3.005	18.0	6.011	25.4	9.016	31.2
412.55	2.38	18–19	S	3.005	17.3	6.011	24.5	9.016	30.0
392.3	2.3	9–12	R	3.160	18.5	6.321	26.2	9.481	32.1
392.23	2.31	8–12	S	3.161	18.6	6.322	26.3	9.483	32.2
419.1[b]	2.52	19–20	R	2.958	17.8	5.917	25.2	8.875	30.8
419.1[b]	2.57	17–20	S	2.958	18.1	5.917	25.7	8.875	31.4

[a] Laser pulse widths ~150 fs, operating at 3 kHz

[b] Used in preliminary study (Ref [10])

Table 2 Legendre Polynomial PAD coefficients, $b_i^{\{p\}}$, and PECD asymmetry, *G*, for R-limonene.

Laser λ	**420.3 nm**	**419.1 nm[a]**	**412.5 nm**	**392.3 nm**	
Selected[b] e⁻ K.E. range	0.1±0.1 eV	0.1±0.1 eV	0.15±0.15 eV	0.38±0.2 eV	1.04±0.2 eV
Non-coincidence data					
$\boldsymbol{b_1^{\{+1\}}}$	-0.026±0.002	-0.023±0.001	-0.022±0.001	-0.009±0.001	0.013±0.001
$\boldsymbol{b_3^{\{+1\}}}$	0.006±0.002	0.000±0.002	0.006±0.001	0.003±0.002	-0.008±0.002
$\boldsymbol{b_5^{\{+1\}}}$	0.002±0.003	0.009±0.002	0.002±0.001	-0.001±0.002	-0.003±0.003
$\boldsymbol{b_2^{\{\pm1\}}}$	-0.206±0.006	-0.122±0.004	-0.202±0.005	-0.193±0.009	-0.123±0.010
$\boldsymbol{b_4^{\{\pm1\}}}$	-0.074±0.008	-0.045±0.006	-0.059±0.007	-0.066±0.012	-0.122±0.014
$\boldsymbol{b_6^{\{\pm1\}}}$	0.070±0.010	-0.012±0.007	0.028±0.009	0.061±0.016	0.054±0.017
***G*(LP)[c]**	-0.054±0.004	-0.044±0.002	-0.047±0.002	-0.020±0.002	0.029±0.003
***G*(F/B)[d]**	-0.053±0.003	-0.044±0.002	-0.046±0.002	-0.019±0.002	0.028±0.003
m/z 136 coincidence filtered data					
$\boldsymbol{b_1^{\{+1\}}}$	-0.035±0.004		-0.029±0.004	-0.012±0.005	0.023±0.010
$\boldsymbol{b_3^{\{+1\}}}$	0.007±0.007		-0.002±0.006	0.006±0.008	-0.024±0.016
$\boldsymbol{b_5^{\{+1\}}}$	0.009±0.009		0.004±0.008	0.018±0.010	-0.016±0.021
$\boldsymbol{b_2^{\{\pm1\}}}$	-0.232±0.007		-0.237±0.006	-0.213±0.010	-0.120±0.011
$\boldsymbol{b_4^{\{\pm1\}}}$	-0.056±0.010		-0.052±0.008	-0.046±0.014	-0.128±0.016
$\boldsymbol{b_6^{\{\pm1\}}}$	0.073±0.013		0.041±0.010	0.084±0.018	0.091±0.021
***G*(LP)**	-0.071±0.010		-0.056±0.009	-0.022±0.010	0.054±0.022
***G*(F/B)**	-0.074±0.010		-0.056±0.008	-0.016±0.011	0.060±0.020

[a] Raw data reported in Ref. [10]

[b] Chosen to span principal peaks in the corresponding PES

[c] Calculated using Eq. 4

[d] Alternative calculation for selected range using Eq. 1

Figures

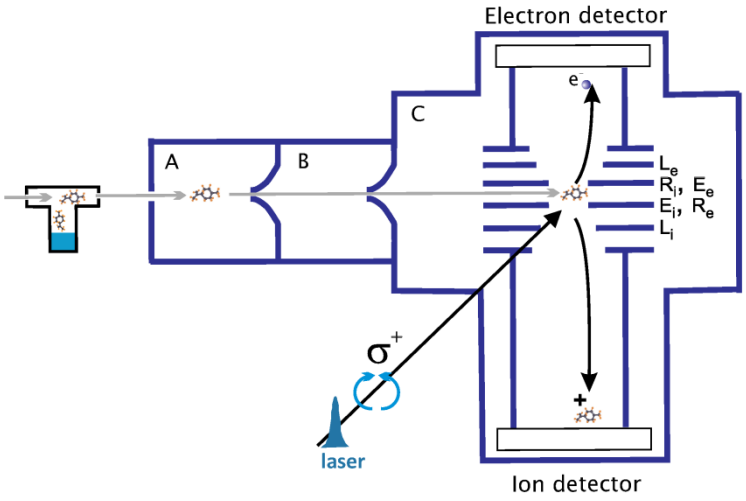

Figure 1. Schematic overview of the experimental setup. Limonene sample is held in a stainless steel reservoir at room temperature. The vapour of limonene is swept into the coincidence machine by pure Ne gas expanding through a small nozzle. The continuous molecular beam resulting is doubly skimmed then intersected by a laser beam. After ionization of the molecule the electron and ion pair is detected in delayed coincidence on two opposing time- and position-sensitive delay line detectors mounted perpendicular to the molecular beam and photon beam. Full details are found in Refs. [20] and [21].

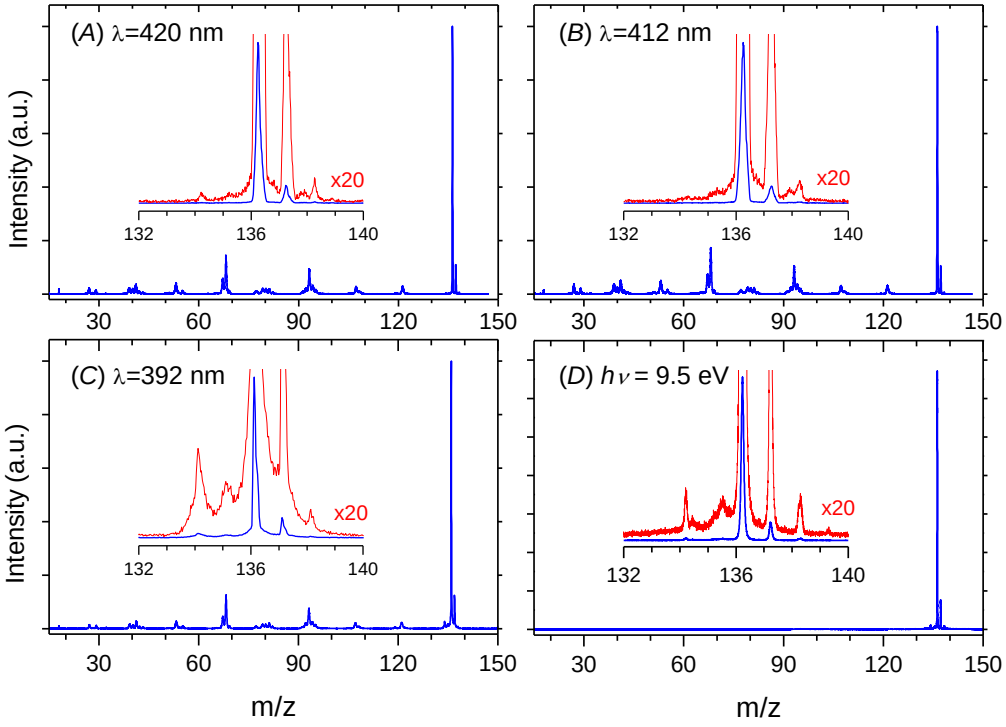

Figure 2. Ion TOF mass spectra recorded under conditions used for PECD measurements. Panels (*A*)–(*C*) use three different laser wavelengths as shown, while (*D*) contains a measurement made with single VUV photon excitation. All panels include an inset showing the TOF expanded around the limonene parent ion mass, 136.2 amu, (blue curve) and with a further ×20 vertical expansion (red curve).

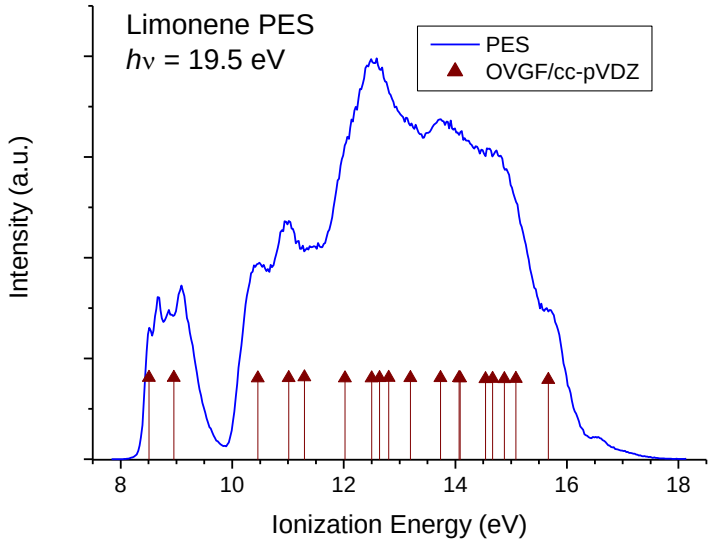

Figure 3. Moderate resolution valence region PES of limonene, recorded with an effusive source. Also marked are vertical ionization energies calculated by outer valence Green's function method using a cc-pVDZ basis.

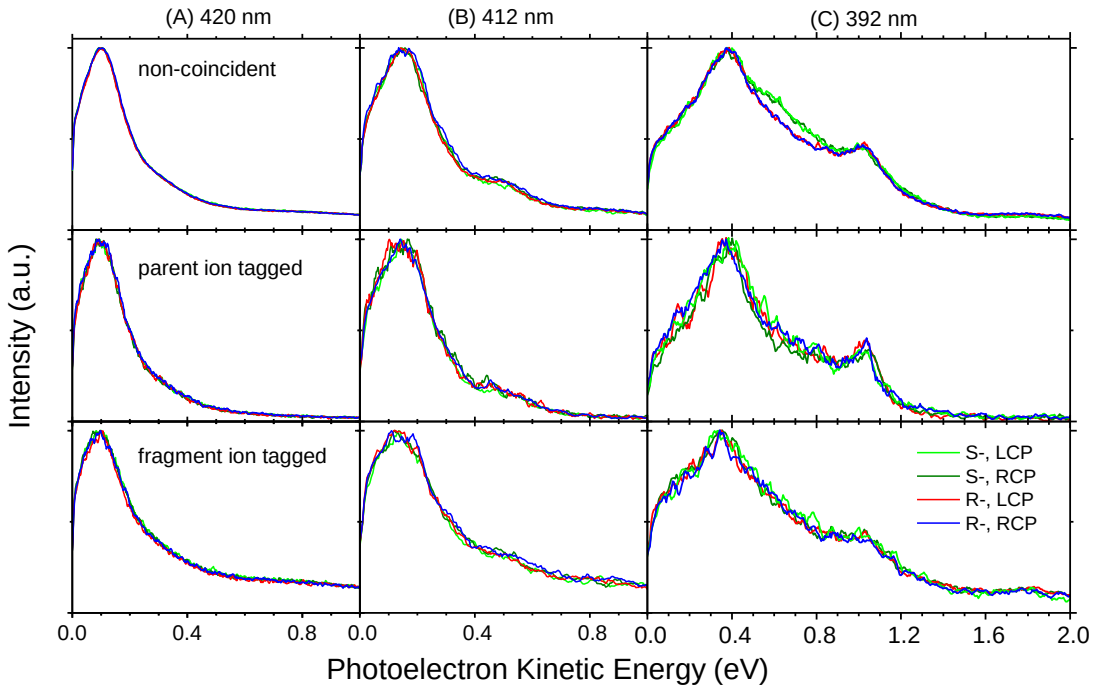

Figure 4. Photoelectron spectra, derived from the recorded 3D electron momenta, measured at 420 nm, 412 nm, and 392 nm, as indicated. A key identifying the various combinations of enantiomer (R/S) and light polarization (RCP/LCP) shown in each panel appears bottom right. The top row of figures show spectra formed from all electrons, without coincidence detection. The middle row shows electron spectra that are coincident with parent ions (m/z = 136), while the bottom row shows spectra that are mass-tagged by coincidence with only fragment ions (m/z < 136) by the coincidence detection.

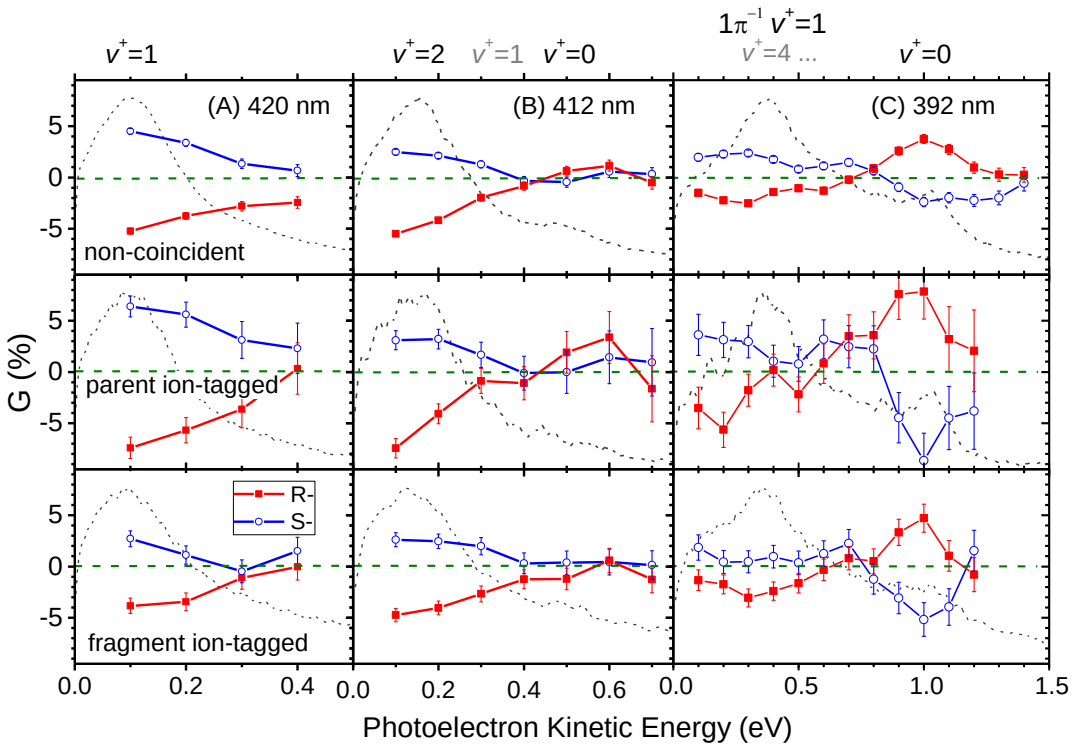

Figure 5. Multiphoton photoelectron circular dichroism asymmetry factors, G, for limonene enantiomers recorded at different wavelengths (columns (*A*)–(*C*)). As in Fig. 3 the top row uses all (non-coincident) electrons, the middle row are electrons coincident with parent ion masses, and the bottom row electrons coincident only with fragment ion masses. Error bars are calculated from Poisson count statistics. Corresponding photoelectron spectra, on a common energy scale, are plotted as grey dashed curves. Above each column are marked indicative cation vibrational level assignments for the observed features (discussed more fully in the text). Unless labelled otherwise these refer to the $2\pi^{-1}$ electronic ground state cation. More tentative assignments are marked in gray.

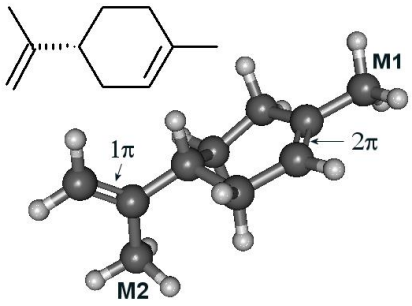

Figure 6. R-limonene in its most stable equatorial conformation. Methyl groups are labelled **M1**, **M2**, to aid discussion in text.

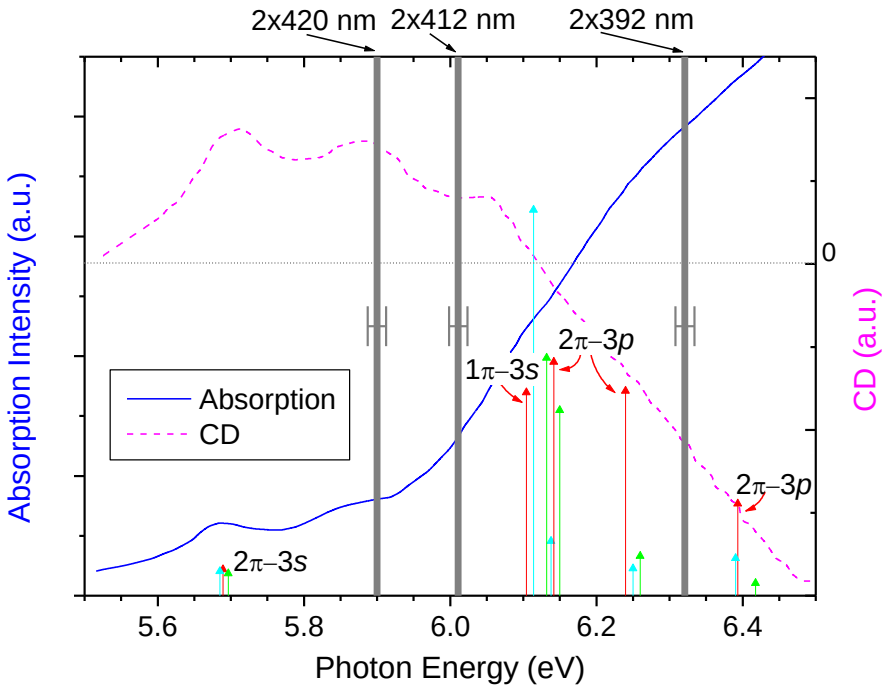

Figure 7. VUV absorption and CD spectra of limonene (Ref. [32]). The positions of Rydberg excitations derived in Ref [10] are indicated, using a colour coding (red, green, cyan) to indicate transitions for the three most stable conformers of limonene (respectively Eq-1, Eq-2, and Eq-3). Also indicated are the two-photon equivalent energies, and estimated 2 photon laser bandwidths, for the three laser wavelengths reported in the current study.

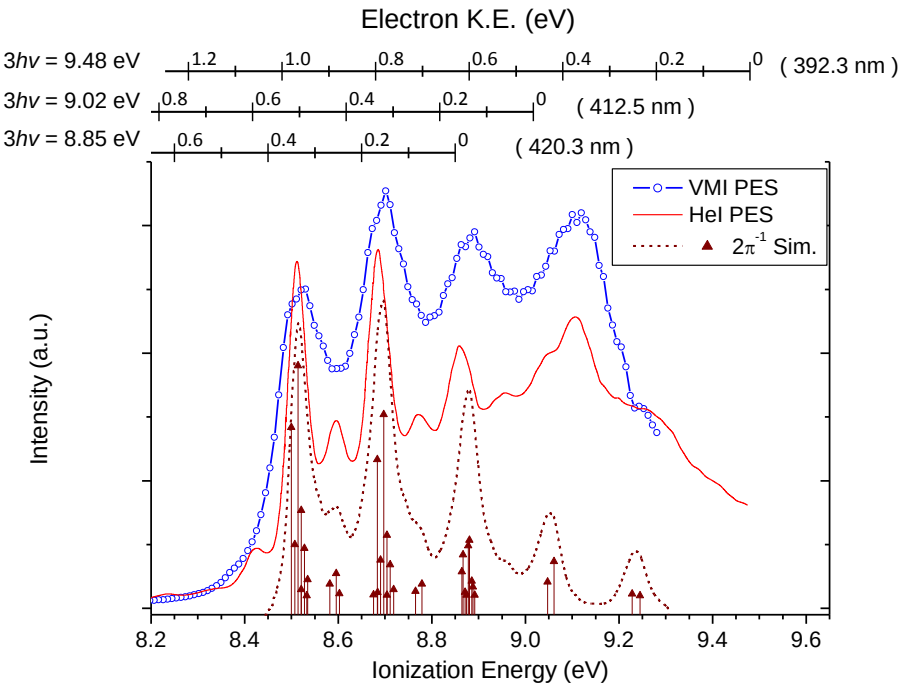

Figure 8. X-band He I photoelectron spectrum of limonene (Ref [27]) and the VUV synchrotron radiation ($h\nu$= 9.5 eV) VMI spectrum (Ref [23]). This region spans the $2\pi^{-1}$ and $1\pi^{-1}$ ionizations. The figure also includes a Franck-Condon vibrational band simulation for the HOMO $2\pi^{-1}$ band using MP2/cc-pVDZ calculations for vibrational analysis of the most stable Eq-1 conformer, with frequencies scaled by a factor of 0.93. For clarity only the most intense transitions are shown in the stick spectrum, while the simulated band profile is a convolution with all transitions included. The width of the latter is chosen to provide a realistic appearance, rather than to match experiment, and has no special significance. Corresponding electron energy scales are marked at the top of this figure with origins set at the three-photon equivalent energies of the wavelengths reported in this study.

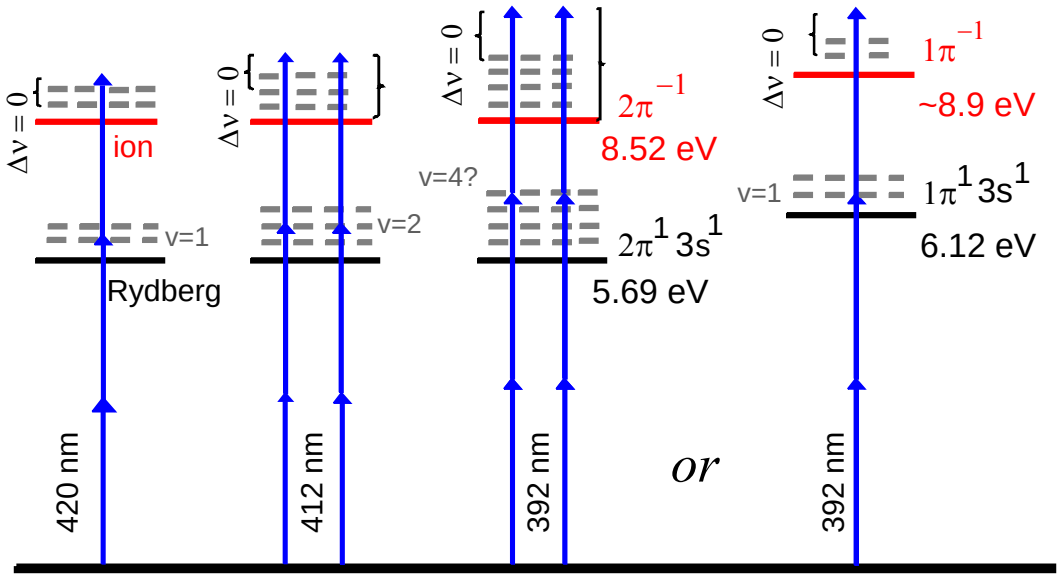

Figure 9. Schematic showing the (2+1) REMPI ionization pathways discussed in the text. For brevity the cation states are labelled by the electron removed ($2\pi^{-1}$, $1\pi^{-1}$) while the Rydberg state designations list just the half-filled orbitals. The braces mark the excess energy appearing as photoelectron kinetic energy for production of the indicated ion vibrational level.

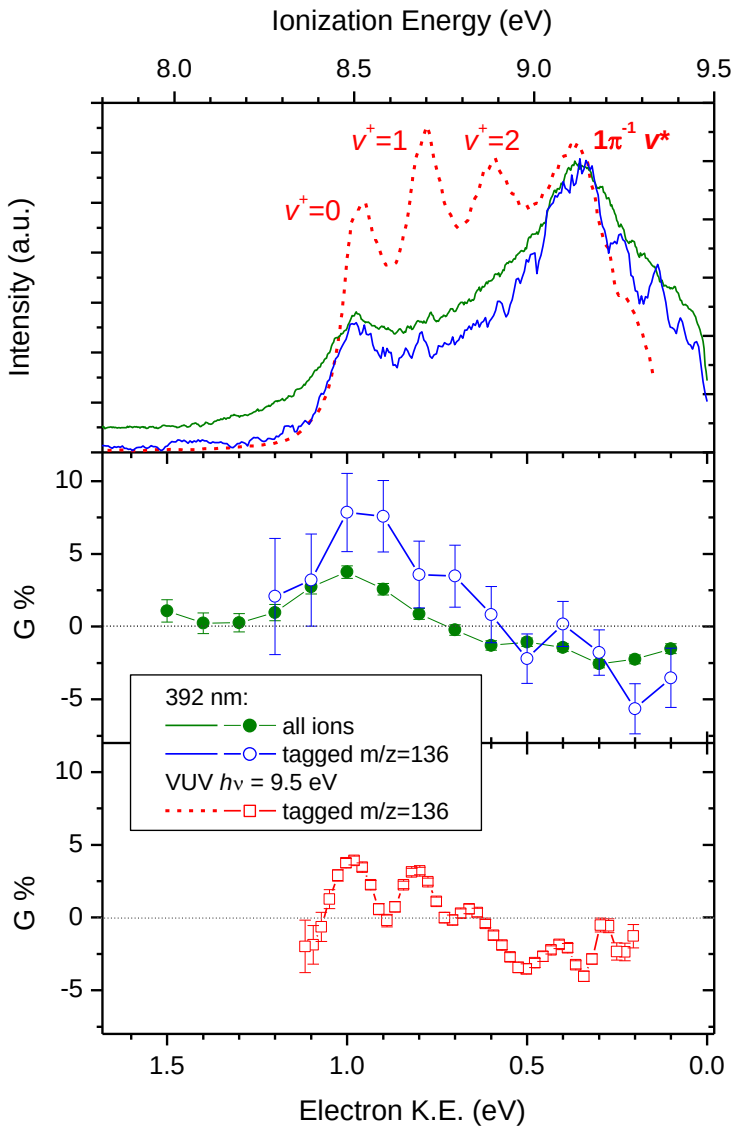

Figure 10. A comparison on a common electron energy axis of the VUV ($h\nu$ = 9.5 eV) single photon ionization data (Ref. [23] and the multiphoton 3×392 nm (equivalent total energy 9.48 eV) results. The top panel provides the PES results and the lower panels include the R-enantiomer PECD data. Labelled assignments shown against the VUV PES peaks are shorthand notation for the more complex structure discussed in the text, but indicate the dominant C=C stretching excitation.